

1-1-2007

## Algorithm Refinement for Fluctuating Hydrodynamics

Alejandro Garcia

*San Jose State University*, [alejandro.garcia@sjsu.edu](mailto:alejandro.garcia@sjsu.edu)

S. Williams

*University of North Carolina at Chapel Hill*

J. B. Bell

*Lawrence Berkeley National Laboratory*

Follow this and additional works at: [https://scholarworks.sjsu.edu/physics\\_astron\\_pub](https://scholarworks.sjsu.edu/physics_astron_pub)



Part of the [Other Astrophysics and Astronomy Commons](#), and the [Other Physics Commons](#)

---

### Recommended Citation

Alejandro Garcia, S. Williams, and J. B. Bell. "Algorithm Refinement for Fluctuating Hydrodynamics" *SIAM Multiscale Modeling and Simulation* (2007): 1256-1280. <https://doi.org/http://dx.doi.org/10.1137/090774501>

This Article is brought to you for free and open access by the Physics and Astronomy at SJSU ScholarWorks. It has been accepted for inclusion in Faculty Publications by an authorized administrator of SJSU ScholarWorks. For more information, please contact [scholarworks@sjsu.edu](mailto:scholarworks@sjsu.edu).

## ALGORITHM REFINEMENT FOR FLUCTUATING HYDRODYNAMICS\*

SARAH A. WILLIAMS<sup>†</sup>, JOHN B. BELL<sup>‡</sup>, AND ALEJANDRO L. GARCIA<sup>§</sup>

**Abstract.** This paper introduces an adaptive mesh and algorithm refinement method for fluctuating hydrodynamics. This particle-continuum hybrid simulates the dynamics of a compressible fluid with thermal fluctuations. The particle algorithm is direct simulation Monte Carlo (DSMC), a molecular-level scheme based on the Boltzmann equation. The continuum algorithm is based on the Landau–Lifshitz Navier–Stokes (LLNS) equations, which incorporate thermal fluctuations into macroscopic hydrodynamics by using stochastic fluxes. It uses a recently developed solver for the LLNS equations based on third-order Runge–Kutta. We present numerical tests of systems in and out of equilibrium, including time-dependent systems, and demonstrate dynamic adaptive refinement by the computation of a moving shock wave. Mean system behavior and second moment statistics of our simulations match theoretical values and benchmarks well. We find that particular attention should be paid to the spectrum of the flux at the interface between the particle and continuum methods, specifically for the nonhydrodynamic (kinetic) time scales.

**Key words.** stochastic Navier–Stokes equations, multiscale hybrid algorithm, computational fluid dynamics, direct simulation Monte Carlo, adaptive mesh refinement

**AMS subject classifications.** 65C30, 60H35, 76M12, 76M28

**DOI.** 10.1137/070696180

**1. Introduction.** Adaptive mesh refinement (AMR) is often employed in computational fluid dynamics (CFD) simulations to improve efficiency and/or accuracy: a fine mesh is applied in regions where high resolution is required for accuracy, and a coarser mesh is applied elsewhere to moderate computational cost. For dynamic problems, the area that is a candidate for mesh refinement may change over time, so methods have been developed to adaptively identify the refinement target area at each time step (e.g., [9, 8, 5]).

However, at the smallest scales, on the order of a molecular mean free path, continuum assumptions may not hold, so CFD approaches do not accurately model the relevant physics. In such a regime, adaptive mesh and algorithm refinement (AMAR) improves on AMR by introducing a more physically accurate particle method to replace the continuum solver on the finest mesh. An improved simulation does not result from continued refinement of the mesh but rather from “refinement” of the algorithm, i.e., switching from the continuum model to a particle simulation. Introduced in [26], AMAR has proved to be a useful paradigm for multiscale fluid modeling. In this paper, we describe AMAR for fluctuating hydrodynamics.

Random thermal fluctuations occur in fluids at microscopic scales (consider Brownian motion), and these microscopic fluctuations can lead to macroscopic sys-

---

\*Received by the editors July 3, 2007; accepted for publication (in revised form) October 24, 2007; published electronically February 1, 2008. This work was supported in part by the Applied Mathematics Program of the DOE Office of Mathematics, Information, and Computational Sciences under the U.S. Department of Energy under contract DE-AC02-05CH11231.

<http://www.siam.org/journals/mms/6-4/69618.html>

<sup>†</sup>Department of Mathematics, University of North Carolina at Chapel Hill, Phillips Hall CB 3250, Chapel Hill, NC 27599 (saw@email.unc.edu).

<sup>‡</sup>Center for Computational Sciences and Engineering, Lawrence Berkeley National Laboratory, 1 Cyclotron Road, MS 50A-1148, Berkeley, CA 94720 (jbbell@lbl.gov).

<sup>§</sup>Department of Physics, San Jose State University, 1 Washington Square, San Jose, CA 95192 (algarcia@algarcia.org).

tem effects. The correct treatment of fluctuations is especially important for stochastic nonlinear systems, such as those undergoing phase transitions, nucleation, noise-driven instabilities, and combustive ignition. In these and related applications, nonlinearities can exponentially amplify the influence of the fluctuations. As an example, consider the classical Rayleigh–Taylor problem and the related Richtmyer–Meshkov instability that are prototypical problems for the study of turbulent mixing. A heavy fluid sits above a light fluid, and spontaneous microscopic fluctuation at the interface between the fluids leads to turbulent mixing throughout the domain. Kadau and coworkers have recently studied the development of this turbulence at the atomic scale [35, 36]. That group’s atomistic simulations indicate that thermal fluctuations are an important driver of the behavior of complex flows, certainly at the smallest scales and perhaps at all scales. For example, in stochastic atomistic simulations of Rayleigh–Taylor, and in laboratory experiments, spikes of the heavy fluid that project into the light fluid can break off to form isolated droplets; this phenomenon cannot be reproduced accurately by deterministic continuum models. However, the physical and temporal domain on which this type of atomistic simulation is computationally feasible is extremely limited (less than a billion atoms per nanosecond) given current algorithms and near-term computational power. Other examples in which spontaneous fluctuations play a key role include the breakup of droplets in nanojets [47, 20, 37], Brownian molecular motors [33, 50, 18, 45], exothermic reactions [49, 41], such as in combustion and explosive detonation, and reaction fronts [46]. The goal of AMAR for fluctuating hydrodynamics is to effectively enhance the computing power available for investigations of these types of phenomena.

Hadjiconstantinou reviewed theoretical and numerical approaches to challenges arising from the breakdown of the Navier–Stokes description at small scale and (with Wijesinghe) described a variety of particle-continuum methods for multiscale hydrodynamics [55, 32]. The work presented here is the latest effort in a line of work that has focused on building AMAR hybrids for flows of increasing sophistication. A hybrid coupling Navier–Stokes and direct simulation Monte Carlo (DSMC) was developed in [26], with several of the technical issues necessary for implementation extended in [56]. Stochastic hybrid methods were developed in [2] (mass diffusion), [3] (the “train model” for momentum diffusion), and [6] (Burgers’s equation). Other recent work on coupling particle and continuum methods includes [53] (DSMC and Navier–Stokes for aerospace applications), [30, 17] (molecular dynamics and isothermal fluctuating hydrodynamics for polymer simulations), and [39] (an adaptive refinement approach based on a direct numerical solution of the Boltzmann transport equation and kinetic continuum schemes).

The AMAR approach is characterized by several design principles. In contrast to other algorithm refinement approaches (see, e.g., [16]), in AMAR (as in AMR) the solution of the macroscopic model is maintained over the entire domain. A refinement criterion is used to estimate where the improved representation of the particle method is required. That region, which can change dynamically, is then “covered” with a particle patch. In this hierarchical representation, upon synchronization the particle solution replaces the continuum solution in the regions covered by the molecular patches.

Given their complexity, the implementations of hybrid codes benefit greatly from modularization (e.g., see [53]). Another fundamental tenet of the AMAR approach to particle-continuum hybridization is that the coupling of the two algorithms is completely encapsulated in several “hand-shaking” routines. Taken as a unit, the particle method plus these modular routines perform exactly the same function as any fine

grid in a single-algorithm AMR method. The encapsulated coupling routines perform the following functions: continuum data is used to generate particles that flow into the particle region; flux across the boundaries of the particle region is recorded and used to correct neighboring continuum values; cell-averaged data from the particle grid replaces data on the underlying continuum grid; continuum data is used to generate particles to initialize new particle regions identified by the refinement criterion.

Implementation details are given in the next two sections of the paper. Our continuum approach for fluctuating hydrodynamics is an explicit finite volume method for solving the Landau–Lifshitz Navier–Stokes (LLNS) equations for compressible fluid flow (see section 2.1) and, as noted above, the particle method is DSMC (see section 2.2). Hybrid coupling details are discussed in section 3. Numerical results for problems with a static refinement region are presented in section 4 for a variety of steady-state and time-dependent problems with the flow restricted to one spatial dimension. (Forthcoming work will illustrate this construction extended to two- and three-dimensional systems.) Details of adaptive refinement are discussed in section 4.5, including numerical results for an adaptive refinement shock-tracking problem. We conclude, in section 5, with a discussion of future work.

## 2. Components of the hybrid.

**2.1. Continuum approach.** The continuum model and solver discussed in this section was introduced in [7], and the reader is referred to that paper for further details of the method and measurements of its performance.

To incorporate thermal fluctuations into macroscopic hydrodynamics, Landau and Lifshitz introduced an extended form of the Navier–Stokes equations by adding stochastic flux terms [40]. The LLNS equations have been derived by a variety of approaches (see [40, 12, 21, 38, 13]), and while they were originally developed for equilibrium fluctuations, validity of the LLNS equations for nonequilibrium systems has been derived [48] and verified in molecular simulations [29, 42, 44].

The LLNS equations may be written as

$$(1) \quad \partial \mathbf{U} / \partial t + \nabla \cdot \mathbf{F} = \nabla \cdot \mathbf{D} + \nabla \cdot \mathbf{S},$$

where

$$\mathbf{U} = \begin{pmatrix} \rho \\ \mathbf{J} \\ E \end{pmatrix}$$

is the vector of conserved quantities (density of mass, momentum, and energy).

The hyperbolic flux is given by

$$\mathbf{F} = \begin{pmatrix} \rho \mathbf{v} \\ \rho \mathbf{v} \mathbf{v} + P \mathbf{I} \\ (E + P) \mathbf{v} \end{pmatrix},$$

and the diffusive flux is given by

$$\mathbf{D} = \begin{pmatrix} 0 \\ \tau \\ \tau \cdot \mathbf{v} + \kappa \nabla T \end{pmatrix},$$

where  $\mathbf{v}$  is the fluid velocity,  $P$  is the pressure,  $T$  is the temperature, and  $\tau = \eta(\nabla \mathbf{v} + \nabla \mathbf{v}^T - \frac{2}{3} \mathbf{I} \nabla \cdot \mathbf{v})$  is the stress tensor. Here  $\eta$  and  $\kappa$  are coefficients of viscosity and thermal conductivity, respectively, where we have assumed that the bulk viscosity is zero.

The mass flux is microscopically exact, but the other two flux components are not; for example, at molecular scales heat may spontaneously flow from cold to hot, in violation of the macroscopic Fourier law. To account for such spontaneous fluctuations, the LLNS equations include a stochastic flux

$$\mathbf{S} = \begin{pmatrix} 0 \\ \mathcal{S} \\ \mathcal{Q} + \mathbf{v} \cdot \mathcal{S} \end{pmatrix},$$

where the stochastic stress tensor  $\mathcal{S}$  and heat flux  $\mathcal{Q}$  have zero mean and covariances given by

$$\begin{aligned} \langle \mathcal{S}_{ij}(\mathbf{r}, t) \mathcal{S}_{kl}(\mathbf{r}', t') \rangle &= 2k_B \eta T \left( \delta_{ik}^K \delta_{jl}^K + \delta_{il}^K \delta_{jk}^K - \frac{2}{3} \delta_{ij}^K \delta_{kl}^K \right) \delta(\mathbf{r} - \mathbf{r}') \delta(t - t'), \\ \langle \mathcal{Q}_i(\mathbf{r}, t) \mathcal{Q}_j(\mathbf{r}', t') \rangle &= 2k_B \kappa T^2 \delta_{ij}^K \delta(\mathbf{r} - \mathbf{r}') \delta(t - t'), \end{aligned}$$

and

$$\langle \mathcal{S}_{ij}(\mathbf{r}, t) \mathcal{Q}_k(\mathbf{r}', t') \rangle = 0,$$

where  $k_B$  is Boltzmann's constant.

For simplification, in this work we restrict our attention to flow in one dimension. That is, we take the fluid velocity  $\mathbf{v} = (u, v, w)$  to be three-dimensional, but we consider spatial derivatives only in the  $x$ -direction. Then (1) simplifies to

$$\begin{aligned} \frac{\partial}{\partial t} \begin{pmatrix} \rho \\ \rho u \\ \rho v \\ \rho w \\ E \end{pmatrix} &= -\frac{\partial}{\partial x} \begin{pmatrix} \rho u \\ \rho u^2 + P \\ \rho uv \\ \rho uw \\ (E + P)u \end{pmatrix} + \frac{\partial}{\partial x} \begin{pmatrix} 0 \\ \tau_{11} \\ \tau_{12} \\ \tau_{13} \\ \tau_{11}u + \tau_{12}v + \tau_{13}w + \kappa \partial_x T \end{pmatrix} \\ (2) \quad &+ \frac{\partial}{\partial x} \begin{pmatrix} 0 \\ s_{11} \\ s_{12} \\ s_{13} \\ q + us_{11} + vs_{12} + ws_{13} \end{pmatrix}, \end{aligned}$$

where  $s_{11}$ ,  $s_{12}$ ,  $s_{13}$ , and  $q$  are independent random variables with zero mean and variances

$$\begin{aligned} \langle s_{11}(x, t) s_{11}(x', t') \rangle &= \frac{8k_B \eta T}{3\sigma} \delta(x - x') \delta(t - t'), \\ \langle s_{12}(x, t) s_{12}(x', t') \rangle &= \frac{2k_B \eta T}{\sigma} \delta(x - x') \delta(t - t'), \\ \langle s_{13}(x, t) s_{13}(x', t') \rangle &= \frac{2k_B \eta T}{\sigma} \delta(x - x') \delta(t - t'), \end{aligned}$$

and

$$\langle q(x, t) q(x', t') \rangle = \frac{2k_B \kappa T^2}{\sigma} \delta(x - x') \delta(t - t'),$$

with  $\sigma$  being the surface area of the system in the  $yz$ -plane.

For the calculations described in this paper we take the fluid to be a dilute gas with equation of state  $P = \rho RT$  (ideal gas law) and energy density  $E = c_v \rho T +$

$\frac{1}{2}\rho(u^2 + v^2 + w^2)$ . The transport coefficients are only functions of temperature; specifically we take them as  $\eta = \eta_0\sqrt{T}$  and  $\kappa = \kappa_0\sqrt{T}$ , where the constants  $\eta_0$  and  $\kappa_0$  are chosen to match the viscosity and thermal conductivity of a hard sphere gas. We also have gas constant  $R = k_B/m$  and  $c_v = \frac{R}{\gamma-1}$ , where  $m$  is the mass of a particle and the ratio of specific heats is taken to be  $\gamma = \frac{5}{3}$ , that is, a monatomic gas. Note that generalizations of fluid parameters are straightforward, and the choice of a monatomic hard sphere gas is for convenience in matching parameters in the PDE with those of DSMC simulations (see section 2.2).

The principal difficulty in solving (2) arises because there is no stochastic forcing term in the mass conservation equation. Accurately capturing density fluctuations requires that the fluctuations be preserved in computing the mass flux. Another key observation is that the representation of fluctuations in CFD schemes is also sensitive to the time step, with extremely small time steps leading to improved results. This suggests that temporal accuracy also plays a significant role in capturing fluctuations. Based on these observations, a discretization aimed specifically at capturing fluctuations in the LLNS equations has been developed [7]. The method is based on a third-order, total variation diminishing (TVD) Runge–Kutta temporal integrator (RK3) [31, 51] combined with a centered discretization of hyperbolic and diffusive fluxes.

The RK3 discretization can be written in the following three-stage form:

$$\begin{aligned}\mathbf{U}_j^{n+1/3} &= \mathbf{U}_j^n - \frac{\Delta t}{\Delta x} (\mathcal{F}_{j+1/2}^n - \mathcal{F}_{j-1/2}^n), \\ \mathbf{U}_j^{n+2/3} &= \frac{3}{4}\mathbf{U}_j^n + \frac{1}{4}\mathbf{U}_j^{n+1/3} - \frac{1}{4} \left( \frac{\Delta t}{\Delta x} \right) (\mathcal{F}_{j+1/2}^{n+1/3} - \mathcal{F}_{j-1/2}^{n+1/3}), \\ \mathbf{U}_j^{n+1} &= \frac{1}{3}\mathbf{U}_j^n + \frac{2}{3}\mathbf{U}_j^{n+2/3} - \frac{2}{3} \left( \frac{\Delta t}{\Delta x} \right) (\mathcal{F}_{j+1/2}^{n+2/3} - \mathcal{F}_{j-1/2}^{n+2/3}),\end{aligned}$$

where  $\mathcal{F}^m = \mathbf{F}(\mathbf{U}^m) - \mathbf{D}(\mathbf{U}^m) - \tilde{\mathbf{S}}(\mathbf{U}^m)$  and  $\tilde{\mathbf{S}} = \sqrt{2}\mathbf{S}$ . The diffusive terms  $\mathbf{D}$  are discretized with standard second-order finite difference approximations. In the approximation to the stochastic stress tensor,  $\tilde{\mathbf{S}}_{j+1/2}$ , the terms are computed as

$$s_{mn} = \sqrt{\frac{k_B}{\Delta t V_c} \left(1 + \frac{1}{3}\delta_{mn}^K\right) (\eta_{j+1}T_{j+1} + \eta_j T_j)} \mathfrak{R}_{j+1/2},$$

where  $V_c = \sigma\Delta x$  is the volume of a cell and the  $\mathfrak{R}$ 's are independent Gaussian distributed random values with zero mean and unit variance. Similarly, the discretized stochastic heat flux is evaluated as

$$q = \sqrt{\frac{k_B}{\Delta t V_c} (\kappa_{j+1}(T_{j+1})^2 + \kappa_j(T_j)^2)} \mathfrak{R}_{j+1/2}.$$

Combining the three stages, we can write

$$\mathbf{U}_j^{n+1} = \mathbf{U}_j^n - \frac{\Delta t}{\Delta x} \left( \mathcal{F}_{j+1/2}^\Sigma - \mathcal{F}_{j-1/2}^\Sigma \right),$$

where

$$\mathcal{F}_{j\pm 1/2}^\Sigma = \frac{1}{6}\mathcal{F}_{j\pm 1/2}^n + \frac{1}{6}\mathcal{F}_{j\pm 1/2}^{n+1/3} + \frac{2}{3}\mathcal{F}_{j\pm 1/2}^{n+2/3}.$$

The variance in the stochastic flux at  $j + 1/2$  is given by

$$\begin{aligned}\langle (\mathbf{S}_{j+1/2}^\Sigma)^2 \rangle &= \left\langle \left( \frac{1}{6}(\tilde{\mathbf{S}}_{j+1/2}^n) + \frac{1}{6}(\tilde{\mathbf{S}}_{j+1/2}^{n+1/3}) + \frac{2}{3}(\tilde{\mathbf{S}}_{j+1/2}^{n+2/3}) \right)^2 \right\rangle \\ &= \left( \frac{1}{6} \right)^2 \langle (\tilde{\mathbf{S}}_{j+1/2}^n)^2 \rangle + \left( \frac{1}{6} \right)^2 \langle (\tilde{\mathbf{S}}_{j+1/2}^{n+1/3})^2 \rangle + \left( \frac{2}{3} \right)^2 \langle (\tilde{\mathbf{S}}_{j+1/2}^{n+2/3})^2 \rangle.\end{aligned}$$

Neglecting the multiplicity in the noise, we obtain the desired result that  $\langle (\mathbf{S}^\Sigma)^2 \rangle = \frac{1}{2} \langle (\tilde{\mathbf{S}})^2 \rangle = \langle (\mathbf{S})^2 \rangle$ ; that is, taking  $\tilde{\mathbf{S}} = \sqrt{2}\mathbf{S}$  corrects for the reduction of the stochastic flux variance due to the three-stage averaging of the fluxes. However, this treatment does not directly affect the fluctuations in density, since the component of  $\mathbf{S}$  in the continuity equation is zero. The density fluctuations are controlled by the spatial discretization. To compensate for the suppression of density fluctuations due to the temporal averaging, we interpolate the momentum  $J = \rho u$  (and the other conserved quantities) from cell-centered values:

$$(3) \quad J_{j+1/2} = \alpha_1(J_j + J_{j+1}) - \alpha_2(J_{j-1} + J_{j+2}),$$

where

$$\alpha_1 = (\sqrt{7} + 1)/4 \quad \text{and} \quad \alpha_2 = (\sqrt{7} - 1)/4.$$

Then in the case in which  $J$  is statistically stationary and constant in space we have exactly  $J_{j+1/2} = J$  and  $\langle \delta J_{j+1/2}^2 \rangle = 2\langle \delta J^2 \rangle$ , as desired; the interpolation is consistent and compensates for the variance-reducing effect of the multistage Runge–Kutta algorithm.

The stochastic flux in our numerical schemes for the LLNS equations is a multiplicative noise since we take variance to be a function of instantaneous temperature. In [7] we tested the importance of the multiplicity of the noise by repeating the equilibrium runs taking the temperature fixed in the stochastic fluxes and found no difference in the results. While this might not be the case for extreme conditions, at that point the hydrodynamic assumptions implicit in the construction of LLNS PDEs would likely also break down; this is yet another reason for using algorithm refinement.

**2.2. Particle approach.** The particle method used here is the direct simulation Monte Carlo (DSMC) algorithm, a well-known method for computing gas dynamics at the molecular scale; see [1, 23] for pedagogical expositions on DSMC, [11] for a complete reference, and [54] for a proof of the method's equivalence to the Boltzmann equation (in the limit that  $N \rightarrow \infty$  while  $\rho$  is constant). As in molecular dynamics, the state of the system in DSMC is given by the positions and velocities of particles. In each time step, the particles are first moved as if they did not interact with each other. After moving the particles and imposing any boundary conditions, collisions are evaluated by a stochastic process, conserving momentum and energy and selecting the postcollision angles from their kinetic theory distributions.

While DSMC is a stochastic algorithm, the statistical variation of the physical quantities has nothing to do with the “Monte Carlo” portion of the method. Equilibrium fluctuations are correctly simulated by DSMC in the same fashion as in molecular dynamics simulations, specifically by the fact that both algorithms produce the correct density of states for the appropriate equilibrium ensembles. For example, for a dilute gas the velocity distribution of the particles is the Maxwell–Boltzmann distribution, and the positions are uniformly distributed. For finite particle number the

DSMC method is closely related to the Kac master equation [34] and the Boltzmann–Langevin equation [12]. For both equilibrium and nonequilibrium problems DSMC yields the physical spectra of spontaneous thermal fluctuations, as confirmed by excellent agreement with fluctuating hydrodynamic theory [27, 42, 29] and molecular dynamics simulations [43, 44].

In this work the simulated physical system is a dilute monatomic hard-sphere gas. For engineering applications more realistic molecular models are regularly used in DSMC; for such a case the construction presented here would be modified only by adjusting the functional form of the transport coefficients and including internal degrees of freedom in the total energy. Our simulation geometry is a rectangular volume with periodic boundary conditions in the  $y$ - and  $z$ -directions. In the  $x$ -direction, Dirichlet (or “particle reservoir”) boundary conditions are used to couple the DSMC domain to the continuum domain of our hybrid method. These interface conditions are described in the next section.

**3. Hybrid implementation.** The fundamental goal of the algorithm refinement hybrid is to represent the fluid dynamics with the low-cost continuum model everywhere except in a localized region where higher-fidelity particle representation is required. In this section, we assume that a fixed refinement region is identified a priori. Additional considerations necessary for dynamic refinement are discussed in section 4.5.

The coupling between the particle and continuum regions uses the analogue of constructs used in developing hierarchical mesh refinement algorithms. The continuum method is applied to the entire computational domain, and a particle region, or patch, is overlaid in refinement regions. For simplicity, in this discussion we will assume that there is a single refined patch. Generalization of the approach to include multiple patches (e.g., [56]) is fairly straightforward.

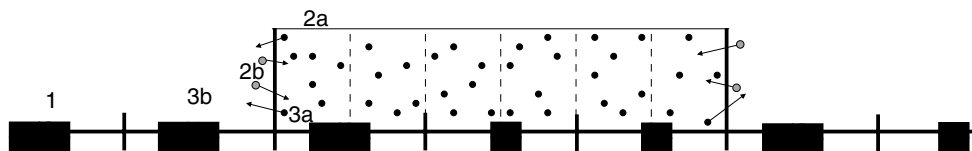


FIG. 1. Schematic representation of the coupling mechanisms of the hybrid algorithm. 1. Advance continuum solution. 2. Advance DSMC solution (2a), using continuum data in reservoir boundaries (2b). 3. Reflux (3a) to correct continuum solution near interface (3b).

Integration on the hierarchy is a three-step process, as depicted in Figure 1. First, we integrate the continuum algorithm from  $t^n$  to  $t^{n+1}$ , i.e., for a continuum step  $\Delta t$ . Next, the particle simulation is advanced to time  $t^{n+1}$ . Continuum data at the edge of the particle patch provides reservoir boundary conditions for the particle method. The implementation of reservoir boundary conditions for DSMC is described in [26]. As in that paper, particles that enter the particle patch have velocities drawn from the either the Maxwell–Boltzmann distribution or the Chapman–Enskog distribution. While the Chapman–Enskog distribution is preferred in deterministic hybrids (see [26]), we find that in the stochastic hybrid the Maxwell–Boltzmann distribution sometimes yields better results for the second moment statistics (see sections 4.1 and 4.3). While Chapman–Enskog yields slightly more accurate results for time-dependent problems, where we focus on the mean behavior of the system (see sections 4.4 and 4.5), one must recall that the derivation of the LLNS equations is based on the assumption of local



equilibrium (e.g., gradients do not appear in the amplitudes of the stochastic fluxes).

When particle velocities in the reservoir cells are generated from the Chapman–Enskog distribution, the gradients of fluid velocity and temperature must be estimated in those cells. Furthermore, we also account for density gradients and generate the particle positions in the reservoir cells accordingly (see the appendix). However, since the fluctuating continuum model generates steep local gradients, even at equilibrium, we use a regional gradient estimate to represent underlying gradient trends. The regional gradient  $D(\xi)$  is implemented as

$$(4) \quad D(\xi)_j = \frac{1}{S\Delta x} \left[ \frac{1}{S} \sum_{i=1}^S \xi_{j+i} - \frac{1}{S} \sum_{i=1}^S \xi_{j-(i-1)} \right],$$

where  $\xi$  is one of the conserved quantities and  $S$  indicates the width of the gradient stencil (we use  $S = 6$ ). Because the Chapman–Enskog distribution is derived from a perturbation expansion in dimensionless gradient, we use slope-limiting to bound the breakdown parameter (see [25] for details).

In general, DSMC uses smaller space and time increments than the continuum method. Spatial refinement is accomplished by dividing the DSMC patch into any number of smaller cells at the collision stage of the algorithm. For simplicity, we assume that an integer number of time steps elapse on the particle patch for every continuum time step. The old and new continuum states,  $U_j^n$  and  $U_j^{n+1}$ , are retained until all the intermediate particle time steps are complete, and the continuum data is interpolated in time to provide appropriate boundary data at each particle method time step. An alternative version of the DSMC algorithm allows the time steps to be event-driven [19], but here we use time increments of fixed size.

Finally, step 3 corrects the macroscopic solution to reflect the effect of the microscopic model as though the integration were tightly coupled. On the region covered by the particle representation we replace the continuum solution by the more accurate particle representation. That is, for each cell covered by the particle patch we set

$$(5) \quad \begin{aligned} \rho_j^{n+1} &= \frac{N_j m}{\sigma \Delta x}, \\ \mathbf{J}_j^{n+1} &= \frac{\sum_{N_j} \mathbf{v} m}{\sigma \Delta x}, \\ E_j^{n+1} &= \frac{\sum_{N_j} \frac{1}{2} (u^2 + v^2 + w^2) m}{\sigma \Delta x}, \end{aligned}$$

where  $N_j$  is the number of particles in cell  $j$ ,  $m$  is the mass of a particle, and  $\sigma \Delta x$  is the volume of a computational cell. In the calculation of each momentum component, the product of the particle mass with the velocity is summed over all particles in the cell. In the calculation of energy we sum the squares of the three velocity components over all the particles in the cell.

Moreover, we must correct (“reflux”) the continuum solution in the cells immediately adjacent to the particle region to account for the gas that entered or exited the particle patch during step 2. Specifically, suppose the leftmost cell of the particle patch is cell  $j + 1$ . The value in continuum cell  $j$  was already updated with the continuum stochastic RK3 scheme, using the total flux,  $\mathcal{F}$ , computed from the continuum values. However, this value is not consistent with the microscopic flux given by the net number of particles moving across edge  $j + 1/2$ . The reflux step corrects the value in cell  $j$  so that it is consistent with the microscopic flux at  $j + 1/2$ .

To perform the refluxing correction we monitor the number of particles,  $N_{j+1/2}^{\rightarrow}$  and  $N_{j+1/2}^{\leftarrow}$ , that move into and out of the particle region, respectively, across the continuum/particle interface at edge  $j + 1/2$ . We then correct the continuum solution as

$$(6) \quad \mathbf{U}_j'^{n+1} = \mathbf{U}_j^{n+1} + \frac{\Delta t}{\Delta x} (\mathcal{F}_{j+1/2}^{\Sigma} - \mathcal{F}_{j+1/2}^{\text{P}}),$$

where the prime indicates the value after the refluxing update. The net particle flux is

$$(7) \quad \mathcal{F}_{j+1/2}^{\text{P}} = \frac{m}{\sigma \Delta t} \begin{pmatrix} N_{j+1/2}^{\rightarrow} - N_{j+1/2}^{\leftarrow} \\ \sum_i^{\rightarrow} \mathbf{v}_i - \sum_i^{\leftarrow} \mathbf{v}_i \\ \frac{1}{2} \sum_i^{\rightarrow} |\mathbf{v}_i|^2 - \frac{1}{2} \sum_i^{\leftarrow} |\mathbf{v}_i|^2 \end{pmatrix},$$

where  $\sum_i^{\rightarrow}$  and  $\sum_i^{\leftarrow}$  are sums over particles crossing the interface from left to right and right to left, respectively.

This update effectively replaces the continuum flux component of the update to  $\mathbf{U}_j^{n+1}$  on edge  $j + 1/2$  by the flux of particles with their associated momentum through the edge. An analogous refluxing step occurs in the cell adjacent to the right-hand boundary of the particle region. Finally, note that this synchronization procedure guarantees conservation. The technical details of refluxing in higher dimensions (e.g., the treatment of corners) are discussed in Garcia et al. [26].

**4. Numerical results.** This section presents a series of computational examples, of progressively increasing sophistication, that demonstrate the accuracy and effectiveness of the algorithm refinement hybrid. First we examine an equilibrium system, then several nonequilibrium examples, concluding with a demonstration of adaptive refinement.

In our testing we compare three numerical schemes: the stochastic scheme based on three-stage Runge–Kutta for the LLNS equations discussed in section 2.1 (*stoch. PDE only*) and two algorithm refinement hybrids as described in section 3. The first hybrid couples DSMC and stochastic RK3 (*stoch. hybrid*). The second hybrid is similar but without a stochastic flux in the LLNS equations; that is, it uses a deterministic version of RK3 (*deter. hybrid*). In some of the tests the results from these schemes are compared with data from a pure DSMC calculation.

The parameters used in the various numerical tests were selected, when possible, to be the same as in [7] to allow for comparison. In that paper it was established that the stochastic RK3 method had a linear convergence of variances in both  $\Delta x$  and  $\Delta t$  and was accurate to within a few percentage points for parameters used here. Furthermore, simulation parameters were chosen to be typical for a DSMC simulation. For example, the time step and cell size truncation errors in DSMC dictate that an accurate simulation requires these to be a fraction of a mean collision time and a mean free path, respectively [11]. The cell volume was selected such that the amplitude of the fluctuations was significant (with a standard deviation of about 10% of the mean) while remaining within the range of validity of fluctuating hydrodynamics.

In principle, the continuum grid of an AMAR hybrid may have as many hierarchical levels as necessary, and there may be many disjoint and/or linked DSMC patches. For simplicity, here we will consider a single DSMC region embedded within a single-level continuum grid. Furthermore, in the following numerical examples we use equal mesh spacing,  $\Delta x$ , and time step size,  $\Delta t$ , in both the continuum and particle methods. The straightforward adjustments necessary for implementing a DSMC grid with smaller  $\Delta x$  and  $\Delta t$  are presented in section 3.

TABLE 1

*System parameters (in cgs units) for simulations of a dilute gas at equilibrium in a periodic domain.*

Molecular diameter (argon)	$3.66 \times 10^{-8}$
Molecular mass (argon)	$6.63 \times 10^{-23}$
Reference mass density	$1.78 \times 10^{-3}$
Reference temperature	273
Specific heat ( $c_v$ )	$3.12 \times 10^6$
Sound speed (c)	30781
Reference mean free path ( $\lambda$ )	$6.26 \times 10^{-6}$
Reference mean free time ( $t_m$ )	$1.64 \times 10^{-10}$
System length	$1.25 \times 10^{-4}$
System volume	$1.96 \times 10^{-16}$
Number of computational cells	40
Cell length ( $\Delta x$ )	$3.13 \times 10^{-6}$
Time step ( $\Delta t$ )	$1.0 \times 10^{-12}$

**4.1. Equilibrium system: State variables.** First, we consider a system in a periodic domain with zero bulk flow and uniform mean energy and mass density. Parameters for this equilibrium system are given in Table 1. Results from this first test problem are depicted in Figures 2–5. For both algorithm refinement hybrids, the particle patch is fixed at the center of the domain, covering cells 15–24, indicated in the figures by vertical dotted black lines. For this equilibrium problem the particles in the patches used to provide boundary reservoirs for DSMC have velocities generated from the Maxwell–Boltzmann distribution. In each simulation the system is initialized near the final state and is allowed to relax for  $5 \times 10^6$  time steps. Statistics are then gathered over  $10^7$  time steps. Note that in these first tests we confirmed that all three schemes conserve total density, momentum, and energy; recall that the hybrids are conservative due to the “refluxing” step.<sup>1</sup>

First, we examine mass density; results from the various numerical schemes are shown in Figure 2. The first panel shows the mean of mass density at each spatial location,  $\langle \rho_i \rangle$ , and the second panel shows the variance,  $\langle \delta \rho_i^2 \rangle = \langle (\rho_i - \langle \rho_i \rangle)^2 \rangle$ . The third panel shows the center-point correlation,  $\langle \delta \rho_i \delta \rho_{j=20} \rangle$ , that is, the covariance of  $\delta \rho_i$  with the value at the center of the domain ( $j = 20$ ). These three quantities are estimated from samples as

$$\begin{aligned}\langle \rho_i \rangle &= \frac{1}{N_s} \sum_{n=1}^{N_s} \rho_i^n, \\ \langle \delta \rho_i^2 \rangle &= \left( \frac{1}{N_s} \sum_{n=1}^{N_s} (\rho_i^n)^2 \right) - \langle \rho_i \rangle^2, \\ \langle \delta \rho_i \delta \rho_{20} \rangle &= \left( \frac{1}{N_s} \sum_{n=1}^{N_s} \rho_i^n \rho_{20}^n \right) - \langle \rho_i \rangle \langle \rho_{20} \rangle,\end{aligned}$$

<sup>1</sup>When the grids move dynamically, this exact conservation is lost because of quantization effects associated with initialization of a particle distribution from continuum data.

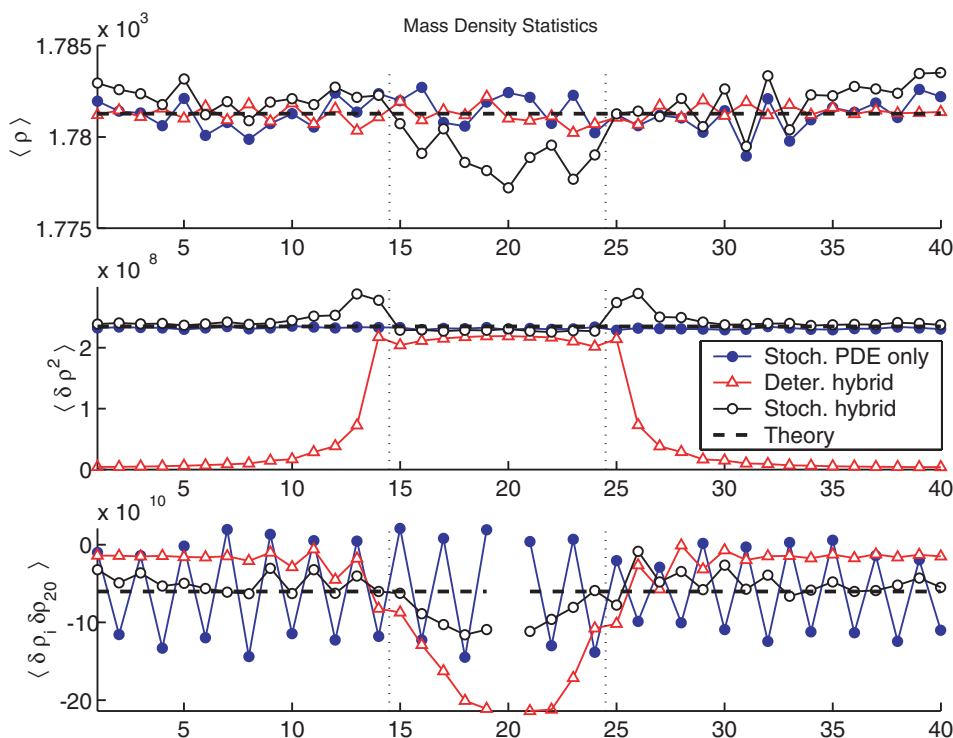


FIG. 2. Mean, variance, and center-point correlation of mass density versus spatial location for a system at equilibrium. Vertical dotted lines depict the boundaries of the particle region for both hybrids. Note that, for clarity, the correlation value at  $i = j = 20$  is omitted from the plot.

where  $N_s = 10^7$  is the number of samples and  $i = 1, \dots, 40$ . Similar statistics for x-momentum, y-momentum, and energy are displayed in Figures 3 and 5; the statistics for z-momentum are similar to those for y-momentum and are omitted here. We consider only these conserved mechanical variables because the continuum scheme is based on them, they are easily measured in molecular simulations, and hydrodynamic variables, such as pressure and temperature, are directly obtained from these mechanical variables [24].

We obtain the correct mean values for all three schemes, with the continuum method exhibiting some numerical oscillations, most notably in the x-momentum. For the most part, the correct variance values are also obtained by the two stochastic schemes. In fact, the stochastic continuum method used here was developed in [7] with the particular goal of correctly reproducing the variances of conserved quantities. Nevertheless, some localized errors in variance introduced by the stochastic hybrid algorithm are evident in these figures. At the left and right boundaries of the particle patch, there is a peak error in the variance of about 23% for mass density and 14% for energy. These discrepancies are discussed in detail in section 4.2.

Figures 2–5 also illustrate the effect on fluctuations when the hybrid’s continuum PDE scheme does not include a stochastic flux. Clearly, the variances drop to near zero inside the deterministic continuum regions, left and right of the particle patch. More significantly, the variances within the patch are also damped. Even more interesting is the appearance of a large correlation of fluctuations in the particle region of the

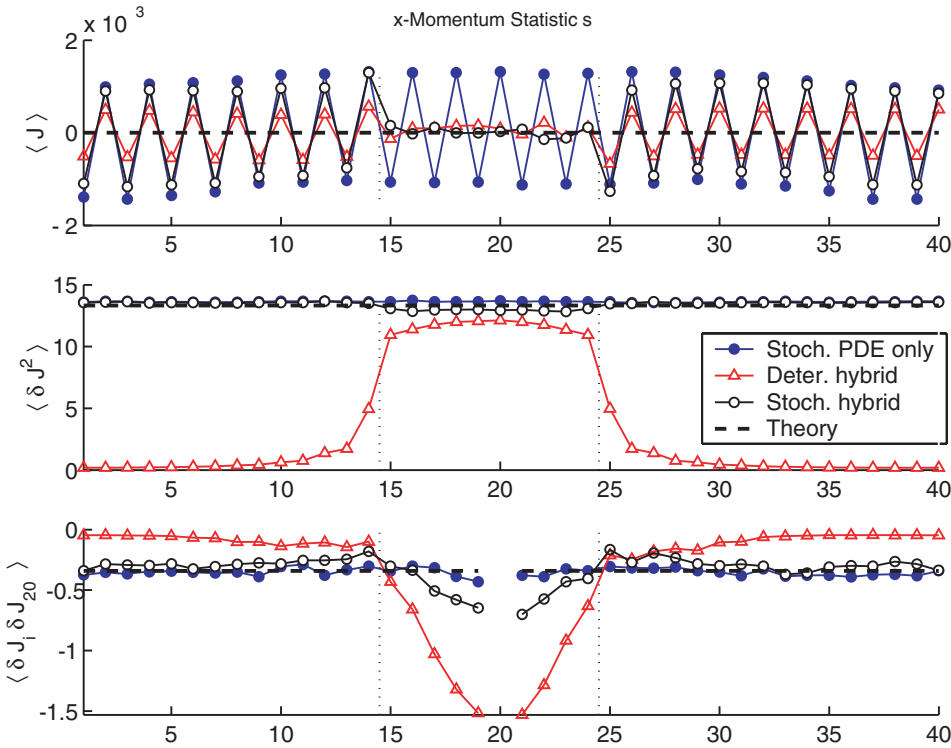


FIG. 3. Mean, variance, and center-point correlation of  $x$ -momentum versus spatial location for a system at equilibrium. Vertical dotted lines depict the boundaries of the particle region for both hybrids. Note that, for clarity, the correlation value at  $i = j = 20$  is omitted from the plot.

deterministic hybrid. It is well known that correlations such as those appearing in the deterministic hybrid are present when a fluid is out of thermodynamic equilibrium (see section 4.3). The results shown here for the center-point correlation in the deterministic hybrid emphasize that the absence of fluctuations in the PDE causes the particle region to be in a nonequilibrium state; similar results were observed in [3, 6]. This result underscores the importance of including fluctuations in the continuum model for problems in which the correct fluctuation structure is needed in the particle region.

**4.2. Equilibrium system: Fluxes.** Ideally, a hybrid method should produce a seamless integration at the interface between two algorithms. However, in section 4.1 we saw that an error arises in the variance of mass density and the variance of energy at algorithm refinement interfaces where the particle method and continuum method interact (see Figures 2 and 5). Furthermore, the spatial correlations, such as  $\langle \delta J_i \delta J_j \rangle$  in Figure 3, exhibit some correlations within the particle region, an effect reminiscent of what is observed in nonequilibrium systems (see section 4.3).

Fluxes are fundamental to the coupling mechanism in AMAR: continuum cells adjacent to a refinement interface are updated with particle flux (see (6)). Therefore, to investigate these errors in the variance, in this section we focus on statistical properties of the flux. We restrict our attention to mass flux, since it is determined by a single factor:  $x$ -momentum in the continuum formulation, as in (2), and number of particle crossings in the discrete formulation, as in (7).

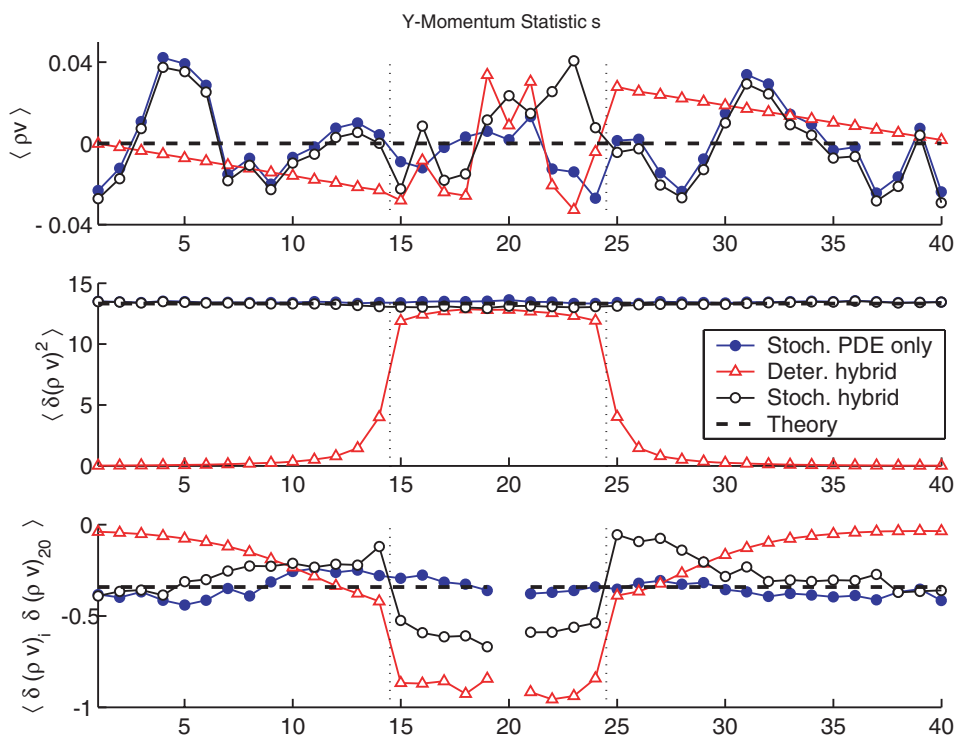


FIG. 4. Mean, variance, and center-point correlation of  $y$ -momentum versus spatial location for a system at equilibrium. Vertical dotted lines depict the boundaries of the particle region for both hybrids. Note that, for clarity, the correlation value at  $i = j = 20$  is omitted from the plot.

In [7] we demonstrated that the stochastic RK3 method and DSMC both obtain the correct means, variances, and correlations, both spatial and temporal, of conserved quantities at equilibrium. Nevertheless, the nature of the fluxes differs markedly between the two methods. To illustrate this point, we consider a pure fluctuating continuum calculation and compare it to a pure DSMC calculation for the same equilibrium test problem discussed in section 4.1.

As shown in Table 2, the variance of  $x$ -momentum,  $\langle \delta J^2 \rangle$ , as obtained by the continuum method and by DSMC, are each in agreement with thermodynamic theory. (Derivation of the theoretically exact variance is discussed in [24].) Hydrodynamic theory directly relates the mass flux to the momentum, and for the stochastic RK3 scheme the variance of mass flux is given by

$$(8) \quad \left\langle \delta F^{(1)^2} \right\rangle = 2 \left( \frac{\Delta t}{\Delta x} \right)^2 \langle \delta J^2 \rangle = 2 \left( \frac{\Delta t}{\Delta x} \right)^2 \frac{\rho k_B T}{\sigma \Delta x}.$$

(See also the discussion of (3).) On the other hand, kinetic theory predicts that the number of particles crossing a cell interface is Poisson distributed, with

$$\langle N^- \rangle = \left\langle (\delta N^-)^2 \right\rangle = \frac{1}{2\sqrt{\pi}} \frac{\rho}{m} \sigma \Delta t \frac{2k_B T}{m}.$$

(Derivation is discussed in [11], for example.) From this we have the variance of the

FIG. 5. Mean, variance, and center-point correlation of energy versus spatial location for a system at equilibrium. Vertical dotted lines depict the boundaries of the particle region for both hybrids. Note that, for clarity, the correlation value at  $i = j = 20$  is omitted from the plot.

TABLE 2  
Variance of  $x$ -momentum and of mass flux at equilibrium.

	$\langle \delta J^2 \rangle$		$\langle \delta F^{(1)^2} \rangle$	
	Stoch. PDE only	DSMC	Stoch. PDE only	DSMC
Computed value	13.62	13.21	2.84E-12	1.44E-10
Thermodynamic theory	13.34	13.34		
Hydrodynamic theory			2.72E-12	
Kinetic theory				1.46E-10
Percentage error	2.1%	-1.0%	4.3%	-1.8%

mass flux given by

$$\begin{aligned}
 \delta F^{(1)^2} &= \frac{m^2}{(\sigma \Delta x)^2} \delta (N^{\rightarrow} - N^{\leftarrow})^2 = \frac{2m^2}{(\sigma \Delta x)^2} (\delta N^{\rightarrow})^2 \\
 (9) \quad &= \frac{m\rho}{\sqrt{\pi}\sigma} \frac{\Delta t}{\Delta x^2} \frac{\overline{2k_B T}}{m}.
 \end{aligned}$$

Comparing (8) and (9), one finds that the hydrodynamic and kinetic theory expressions match when the Courant number,  $C = c\Delta t/\Delta x$ , is order one, yet for the runs presented here  $C \approx 10^{-2}$  (see Table 1).

From Table 2, we see that the variance of the mass flux for the continuum method is in good agreement with the hydrodynamic theory (see (8)), and the corresponding

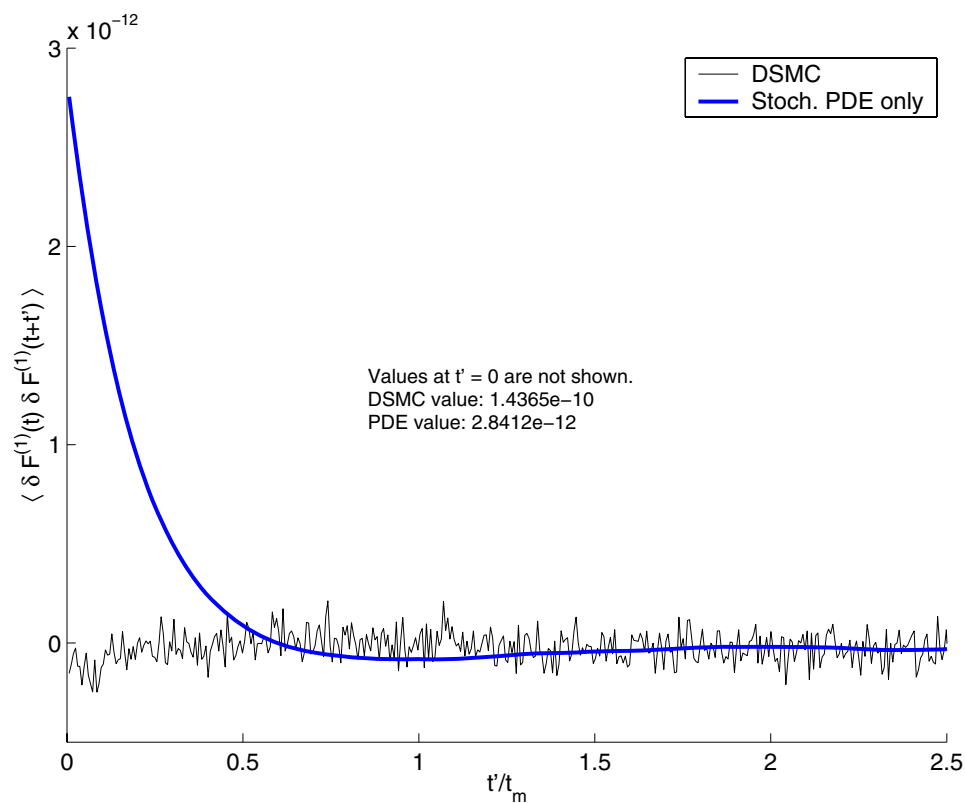


FIG. 6. Time correlations of mass flux for the particle method (DSMC) and the PDE method.

DSMC result is in good agreement with kinetic theory (see (9)). Yet, the two variances of mass flux differ by over two orders of magnitude. To understand the nature of this discrepancy, we investigate the time correlation of the mass flux.

To estimate the time correlation of mass flux for a timeshift of  $t'$ , we calculate  $\langle \delta F^{(1)}(t) \delta F^{(1)}(t + t') \rangle$  in each of the 40 computational cells from approximately  $10^5$  data samples. The average value of each time correlation over the 40 computational cells is displayed in Figure 6 for stochastic RK3 and for DSMC. Time correlation data is displayed in units of mean free collision time ( $t_m$ ).

In Figure 6 we see that the mass flux for DSMC decorrelates immediately, whereas the continuum mass flux decorrelates after approximately one half of one mean free collision time. Note that for all the simulation results presented here, the stochastic PDE and the DSMC use the same time step, and that time step is over two orders of magnitude smaller than  $t_m$ . The origin of the discrepancy in Table 2 is now clear. The hydrodynamic formulation is accurate only at hydrodynamic time scales, that is, at time scales that are large compared to  $t_m$ . Further investigations (not presented here) indicate that when the two methods are run using a significantly larger time step, the variance and time correlations of the mass flux are in general agreement between the two methods. However, at large time step, the truncation error for the PDE scheme negatively affects the results for other quantities, e.g., the variance in conserved quantities. Given that the statistical properties of the fluxes differ between hydrodynamic scales and molecular (kinetic) scales, it is not surprising



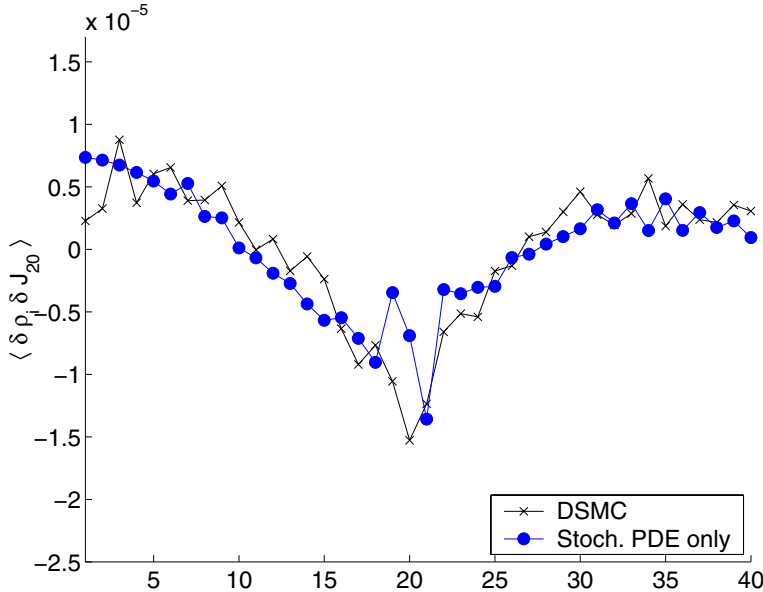


FIG. 7. Center-point correlation of mass density and  $x$ -momentum for a system under a steep temperature gradient.

that the variances of conserved quantities are not seamless at the interface of the two methods and a spatial correlation of these quantities is observed. Why the former effect is most prominent for density and energy variances is still under investigation. This issue is discussed further in the concluding section.

**4.3. Nonequilibrium system: Temperature gradient.** In the early 1980's, a variety of statistical mechanics calculations predicted that a fluid under a non-equilibrium constraint, such as a temperature gradient, would exhibit long-range correlations of fluctuations [52, 15]. Due to the asymmetry of sound waves moving parallel versus antiparallel to the temperature gradient, quantities that are independent at equilibrium, such as density and momentum fluctuations, also have long-range correlations. These predictions were qualitatively confirmed by light scattering experiments [10], yet the effects are subtle and difficult to measure accurately in the laboratory. Molecular simulations confirm the predicted correlations of non-equilibrium fluctuations for a fluid subjected to a temperature gradient [22, 42] and to a shear [28]; they are also observed in simple random walk models of fluids [3]. With these predictions in mind, we consider a system with a temperature gradient. Specifically, the boundary conditions are thermal walls at 273K and 819K; the other system parameters are as shown in Table 1. This nonequilibrium state is extreme, with a temperature gradient of millions of degrees per centimeter, yet it is accurately modeled by DSMC, which was originally developed to simulate strong shock waves.

The system is initialized near the final state and is allowed to relax for  $10^6$  time steps before samples are taken at each computational cell over  $10^8$  time steps. The measure shown here (Figures 7–9) is the spatial correlation between mass density and momentum, specifically  $\langle \delta \rho_i \delta J_{20} \rangle$ . A pure DSMC simulation is used as the benchmark.

Although the stochastic RK3 method gives a good match to the DSMC benchmark away from the correlation point, the results deteriorate near the correlation point

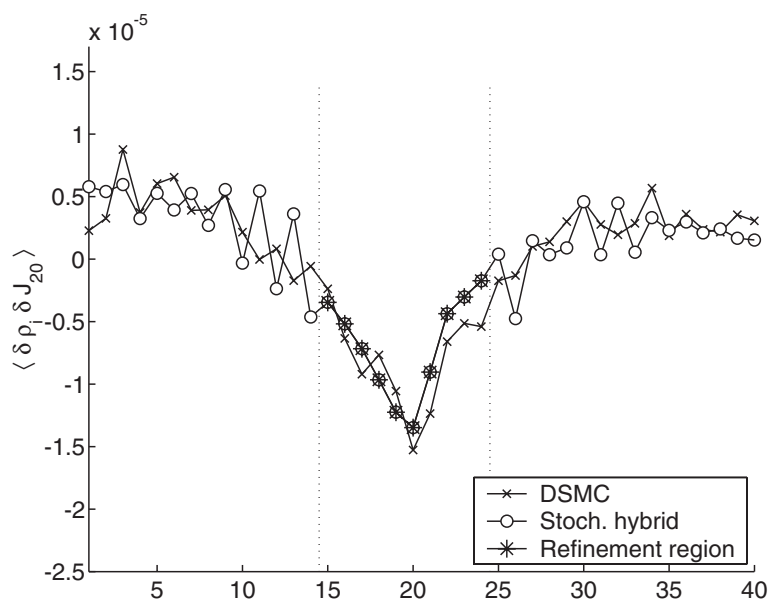


FIG. 8. Center-point correlation of mass density and  $x$ -momentum for a system under a steep temperature gradient. Vertical dotted lines depict the boundaries of the particle region for the hybrid method.

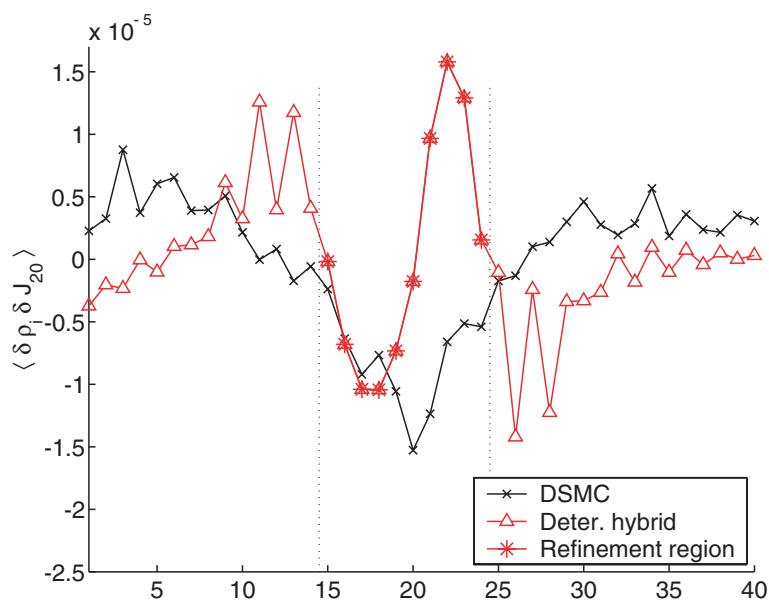


FIG. 9. Center-point correlation of mass density and  $x$ -momentum for a system under a steep temperature gradient. Vertical dotted lines depict the boundaries of the particle region for the hybrid method.

(Figure 7). In the stochastic hybrid method, a particle patch is placed around the region of difficulty, and the results are significantly improved in that region (Figure 8). Given that theoretical results often make predictions for the near-center-point

TABLE 3

*System parameters (in cgs units) for simulations of a traveling shock.*

Mach number	2.0	
	LHS	RHS
Mass density	$4.07 \times 10^{-3}$	$1.78 \times 10^{-3}$
Velocity (x-direction)	34629	0
Temperature	567	273
Sound speed	44373	30781
Mean free path	$2.74 \times 10^{-6}$	$6.26 \times 10^{-6}$
Cell length ( $\Delta x$ )	$3.13 \times 10^{-6}$	
Time step ( $\Delta t$ )	$1.0 \times 10^{-12}$	

correlations (e.g.,  $\langle \delta \rho_i \delta J_j \rangle \propto \nabla T$  for  $i \approx j$ ), making it the region of interest, the stochastic hybrid method outperforms the pure continuum method in this nonequilibrium test case. Finally, in Figure 9 we consider the hybrid that couples deterministic RK3 with DSMC. Again, DSMC is employed in a single patch at the center of the domain. However, with fluctuations suppressed in the remainder of the domain, the overall results suffer. Strikingly, the results suffer not only in the continuum region but also within the particle region.

**4.4. Nonequilibrium system: Strong moving shock.** In this time-dependent problem, we consider a Mach 2 shock traveling through a domain that includes a static refinement region. The objective of this example is to test how well the hybrid performs when a strong nonlinear wave crosses the interface between continuum and particle regions. Dirichlet boundary conditions are used at the domain boundaries; values for the left-hand state (LHS) and right-hand state (RHS) are given in Table 3.

The mass density profile depicted by the dark line is an average profile from an ensemble of 2000 stochastic hybrid runs. Results from an ensemble of 2000 pure stochastic PDE simulations of the traveling wave, without a particle patch, are shown for comparison. The first panel of Figure 10 also includes the mass density profile from a single stochastic hybrid simulation, illustrating the relative magnitude of the thermal fluctuations. At time  $t_0$ , before the shock enters the particle region, the ensemble-averaged data is smooth. At time  $t_1$ , a spurious reflected wave is formed at the interface on the left-hand side of the particle patch. This spurious acoustic wave is damped as it propagates leftward, vanishing by time  $t_4$ . Another small error effect is seen as the shock exits the particle patch, at time  $t_5$ , but it is barely discernible by time  $t_7$ . In summary, we observe a relatively local and short-lived error that indicates an impedance mismatch between the continuum and particle regions, as shown in Figure 10. This mismatch is likely due to the linear approximation of the shear stress and heat flux in the Navier–Stokes equations, which is not accurate for the steep gradients of a strong shock. More complicated expressions for the dissipative fluxes have been derived (e.g., Burnett equations [14]), but for a variety of reasons, such as difficulties in treating boundary conditions, they are not in common use in CFD.

A well-known feature of CFD solvers is the artificial steepening of viscous shock profiles; it is also well established that DSMC predicts shock profiles accurately [11, 4]. At times  $t_2$  through  $t_6$ , we see a steepness discrepancy between the ensemble hybrid profile and the ensemble PDE-only profile. Within the particle patch, the DSMC algorithm correctly resolves a more shallow profile. This example demonstrates the robustness and stability of the treatment of the interface between the particle region and the continuum solver.

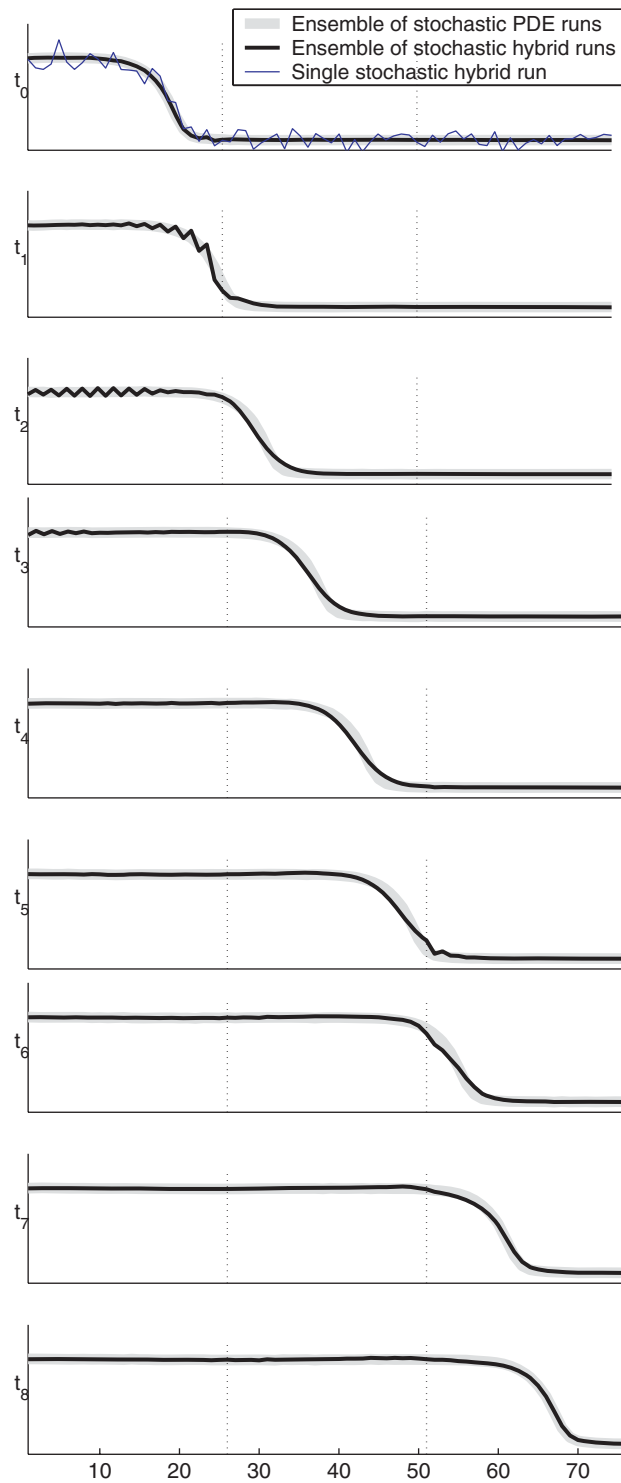


FIG. 10. Mass density profiles for a viscous shock wave traveling through a fixed refinement region (indicated by vertical dotted lines). The time elapsed between each panel is  $300\Delta t$ ; see Table 3 for system parameters.

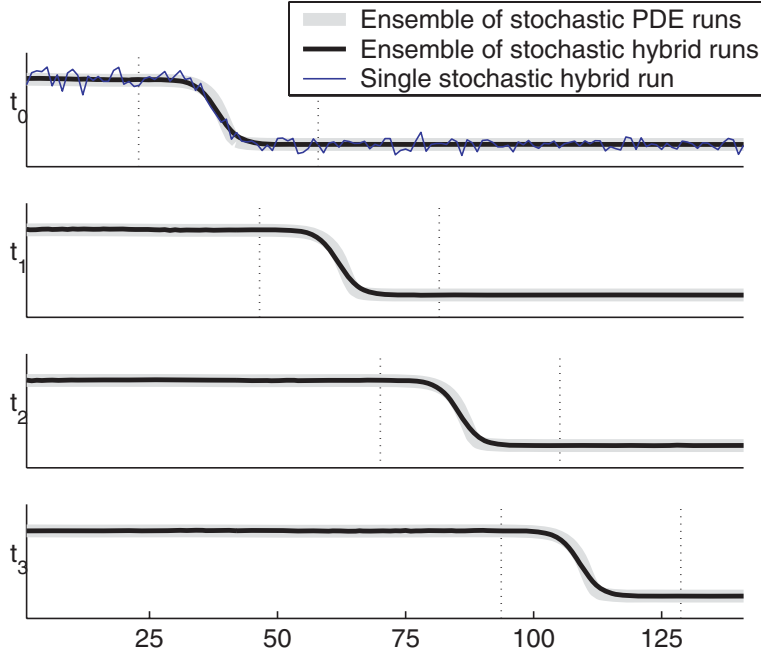


FIG. 11. Mass density profiles for a viscous shock wave, demonstrating AMR: The refinement region, indicated by vertical dotted lines, is determined dynamically at runtime. The time elapsed between each panel is  $1200\Delta t$ ; see Table 3 for system parameters.

Finally, in this example, the Chapman–Enskog distribution was used to initialize velocities of particles that enter the refinement region from the continuum region. This approach was found to result in a somewhat reduced impedance mismatch compared to the Maxwell–Boltzmann distribution.

**4.5. Adaptive refinement.** The final numerical test demonstrates the adaptive refinement capability of our hybrid algorithm. As in section 4.4, a strong traveling shock (Mach 2) moves through a domain with Dirichlet boundary conditions; system parameters are given in Table 3. Here, though, the location of a particle patch is determined dynamically by identifying cells in which the gradient of pressure exceeds a given tolerance; the particle patch is shown in Figure 11 by vertical dotted lines.

Large scale gradients in pressure provide an effective criterion for identifying the presence of a shock wave. Since the fluctuations produce steep localized gradients nearly everywhere, a regional gradient measure,  $D(P)$ , is employed to detect these strong gradients. This is implemented as

$$D(P)_j = \frac{1}{S\Delta x} \left( \frac{1}{S} \sum_{i=1}^S P_{j+i} - \frac{1}{S} \sum_{i=1}^S P_{j-(i-1)} \right),$$

where  $S$  indicates the width of the gradient stencil (we use  $S = 6$ ). For an equilibrium system, the expected variance of  $D(P)$  is estimated by

$$\langle \delta D(P)^2 \rangle = \frac{2}{S^3 \Delta x^2} (\langle \delta \rho^2 \rangle R^2 T_0^2 + \rho_0^2 R^2 \langle \delta T^2 \rangle) = \frac{10}{3} \frac{1}{S^3 N_c} \left( \frac{P_0}{\Delta x} \right)^2,$$

where  $\rho_0$ ,  $T_0$ , and  $P_0$  are the reference mass density, temperature, and pressure for the system and  $N_c$  is the number of particles in a cell at reference conditions. (This variance can be found using the ideal gas law and expressions derived in [24].) Note that using a wide stencil limits the variation even when  $N_c$  is small (and, consequently, fluctuations are large). We select cells  $j$  for refinement where  $D(P)_j$  exceeds the equilibrium value, namely zero, by three standard deviations. The resulting particle patch is extended by a buffer of four cells on each side.

In this implementation, we re-evaluate the location of the particle patch every 100 time steps. When the extent of the refinement region changes, some continuum cells may be added to the DSMC patch, some DSMC cells may become continuum cells, and some DSMC cells may remain in the refinement patch. For continuum cells that are added to the DSMC patch, particles are initialized from the underlying continuum data, as in the case of a static patch. For DSMC cells that should no longer be included in the refinement patch, particle data is averaged onto the continuum grid, as in (5), then discarded. For those DSMC cells that remain in the particle patch, the particle data is retained.

The mass density profile depicted by the dark line is an average profile from an ensemble of 2000 stochastic hybrid runs. The first panel of Figure 11 also includes the mass density profile from a single stochastic hybrid simulation, illustrating the relative magnitude of the thermal fluctuations. Results from an ensemble of 2000 pure stochastic PDE simulations of the traveling wave, without a particle patch, are also shown for comparison. As in Figure 10, we show that a more shallow profile is captured by the DSMC representation of the viscous shock (i.e., by the hybrid that uses DSMC in the vicinity of the shock) versus the artificially steep profile produced by the PDE-only system.

**5. Conclusions and further work.** We have constructed a hybrid algorithm that couples a DSMC molecular simulation with a new numerical solver for the LLNS equations for fluctuating compressible flow. The algorithm allows the particle method to be used locally to approximate the solution while modeling the system using the mean field equations in the remainder of the domain. In tests of the method we have demonstrated that it is necessary to include the effect of fluctuations, represented as a stochastic flux, in the mean field equations to ensure that the hybrid preserved key properties of the system. As expected, not representing fluctuations in the continuum regime leads to a decay in the variance of the solution that penetrates into the particle region. Somewhat more surprising is that the failure to include fluctuations was shown to introduce spurious correlations of fluctuations in equilibrium simulations.

The coupling of the particle and continuum algorithms presented here is not entirely seamless for the variance and correlations of conserved quantities. The mismatch appears to be primarily caused by the inability of the continuum stochastic PDE to reproduce the temporal spectrum of the particle fluxes at kinetic time scales. This is not so much a failure of the methodology as much as a fundamental difference between molecular and hydrodynamic scales. With this caveat, one still finds that using a stochastic PDE in an AMAR hybrid yields significantly better fidelity in the fluctuation variances and correlations, making it useful for applications such as those described in the introduction.

There are several directions that we plan to pursue in future work. As a first step, we plan to extend the methodology to two- and three-dimensional hybrids. The key algorithmic steps developed here extend naturally to multiple dimensions. For more general applications, an overall approach needs to be implemented to support particle

regions defined by a union of nonoverlapping patches. Another area of development is to include additional physical effects in both the continuum and particle models. As a first step in this direction, it is straightforward to include the capability to model different species. This provides the necessary functionality needed to study Rayleigh–Taylor instabilities and other mixing phenomena. A longer term goal along these lines would be to include chemical reactions within the model to enable the study of ignition phenomena. Finally, we note that the results presented here suggest a number of potential improvements to the core methodology. Of particular interest in this area would be approaches to the fluctuating continuum equations that can accurately capture fluctuations while taking a larger time step. This would not only improve the efficiency of the methodology, it would also enable the continuum solver to take time steps at hydrodynamic time scales which should serve to improve the quality of coupling between continuum and particle regions.

#### Appendix. Random placement of particles with a density gradient.

Consider the problem of selecting a random position for a particle within a rectangular cell. The density in the cell varies linearly with  $\rho_0$  being the density at the center (which is also the mean density). For a cell with dimensions  $\Delta x$ ,  $\Delta y$ , and  $\Delta z$ , taking the origin at the corner of the cell we have

$$\rho(x, y, z) = \rho_0 + a_x(x - \Delta x/2) + a_y(y - \Delta y/2) + a_z(z - \Delta z/2),$$

where  $a_x = \partial\rho/\partial x$ . The probability that a particle has position component  $x$  is

$$P(x) = \frac{\int_0^{\Delta y} dy \int_0^{\Delta z} dz \rho(x, y, z)}{\rho_0 \Delta x \Delta y \Delta z} = \frac{1 + \gamma_x(x/\Delta x - \frac{1}{2})}{\Delta x},$$

where  $\gamma_x \equiv \Delta x a_x / \rho_0$ . It will be more convenient to work in the dimensionless variable  $X = x/\Delta x$ . Since  $P(x) dx = P(X) dX$ ,

$$P(X) = 1 + \gamma_x \left( X - \frac{1}{2} \right).$$

By the method of inversion [23] one may generate random values from this distribution by

$$X = \gamma_x^{-1} \left[ (\gamma_x/2 - 1) + [(\gamma_x/2 - 1)^2 + 2\gamma_x \mathcal{R}]^{1/2} \right],$$

where  $\mathcal{R}$  is a random value uniformly distributed in  $[0, 1]$ . The reader is cautioned that the above is susceptible to round-off error for  $\gamma_x \approx 0$  (i.e., small gradient case). Note that in that limit,

$$X \approx \frac{\mathcal{R}}{1 - \gamma_x/2},$$

from which we recover the expected result that  $X = \mathcal{R}$  when  $\gamma_x = 0$ .

The selection of the  $y$  component of the position is complicated by the fact that it is *not* independent of the  $x$  component. The conditional probability of the  $y$  component of position is

$$P(y|x) = \frac{P(x, y)}{P(x)} = \frac{1}{\Delta y} \left[ 1 + \frac{\Delta y a_y / \rho_0}{1 + (\Delta x a_x / \rho_0)(x/\Delta x - \frac{1}{2})} \left( \frac{y}{\Delta y} - \frac{1}{2} \right) \right].$$

Define  $\gamma_y \equiv \Delta y a_y / \rho_0$  and  $Y \equiv y / \Delta y$ ; then

$$P(Y|X) = 1 + \frac{\gamma_y}{P(X)} \left( Y - \frac{1}{2} \right).$$

Fortunately, after selecting  $X$  the selection of  $Y$  is simple;  $Y$  is generated in the same way as  $X$  but with  $\gamma_y/P(X)$  in place of  $\gamma_x$ .

Finally, to select the  $z$  component of the position the procedure is similar to

$$P(Z|X, Y) = 1 + \frac{\gamma_z}{P(X, Y)} \left( Z - \frac{1}{2} \right),$$

where  $P(X, Y) = P(X|Y)P(Y) = 1 + \gamma_x(X - \frac{1}{2}) + \gamma_y(Y - \frac{1}{2})$ . Again, the  $z$  component can be generated in the same way as the  $x$  component but with  $\gamma_z/P(X, Y)$  replacing  $\gamma_x$ .

#### REFERENCES

- [1] F. J. ALEXANDER AND A. L. GARCIA, *The direct simulation Monte Carlo method*, Computers in Physics, 11 (1997), pp. 588–593.
- [2] F. J. ALEXANDER, A. L. GARCIA, AND D. M. TARTAKOVSKY, *Algorithm refinement for stochastic partial differential equations: I. Linear diffusion*, J. Comput. Phys., 182 (2002), pp. 47–66.
- [3] F. J. ALEXANDER, A. L. GARCIA, AND D. M. TARTAKOVSKY, *Algorithm refinement for stochastic partial differential equations: II. Correlated systems*, J. Comput. Phys., 207 (2005), pp. 769–787.
- [4] H. ALSMEYER, *Density profiles in argon and nitrogen shock waves measured by the absorption of an electron beam*, J. Fluid Mech., 74 (1976), pp. 497–513.
- [5] J. B. BELL, M. BERGER, J. SALTZMAN, AND M. WELCOME, *Three-dimensional adaptive mesh refinement for hyperbolic conservation law*, SIAM J. Sci. Comput., 15 (1994), pp. 127–138.
- [6] J. B. BELL, J. FOO, AND A. GARCIA, *Algorithm refinement for the stochastic Burgers' equation*, J. Comput. Phys., 223 (2007), pp. 451–468.
- [7] J. B. BELL, A. L. GARCIA, AND S. A. WILLIAMS, *Numerical methods for the stochastic Landau-Lifshitz Navier-Stokes equations*, Phys. Rev. E (3), 76 (2007), 016708.
- [8] M. BERGER AND P. COLELLA, *Local adaptive mesh refinement for shock hydrodynamics*, J. Comput. Phys., 82 (1989), pp. 64–84.
- [9] M. BERGER AND J. OLIGER, *Adaptive mesh refinement for hyperbolic partial differential equations*, J. Comput. Phys., 53 (1984), pp. 484–512.
- [10] D. BEYSENS, Y. GARRABOS, AND G. ZALCZER, *Experimental evidence for Brillouin asymmetry induced by a temperature gradient*, Phys. Rev. Lett., 45 (1980), pp. 403–406.
- [11] G. A. BIRD, *Molecular Gas Dynamics and the Direct Simulation of Gas Flows*, Clarendon, Oxford, UK, 1994.
- [12] M. BIXON AND R. ZWANZIG, *Boltzmann-Langevin equation and hydrodynamic fluctuations*, Phys. Rev., 187 (1969), pp. 267–272.
- [13] E. CALZETTA, *Relativistic fluctuating hydrodynamics*, Classical Quantum Gravity, 15 (1998), pp. 653–667.
- [14] S. CHAPMAN AND T. G. COWLING, *The Mathematical Theory of Non-Uniform Gases*, Cambridge University Press, Cambridge, UK, 1991.
- [15] J. M. ORTIZ DE ZARATE AND J. V. SENGERS, *Hydrodynamic Fluctuations in Fluids and Fluid Mixtures*, Elsevier Science, Amsterdam, 2007.
- [16] R. DELGADO-BUSCALIONI AND P. V. COVENEY, *Continuum-particle hybrid coupling for mass, momentum, and energy transfers in unsteady fluid flow*, Phys. Rev. E (3), 67 (2003), 046704.
- [17] R. DELGADO-BUSCALIONI AND G. DE FABRITIIS, *Embedding molecular dynamics within fluctuating hydrodynamics in multiscale simulations of liquids*, Phys. Rev. E (3), 76 (2007), 036709.
- [18] C. VAN DEN BROECK, R. KAWAI, AND P. MEURS, *Exorcising a Maxwell demon*, Phys. Rev. Lett., 93 (2004), 090601.
- [19] A. DONEV, A. L. GARCIA, AND B. J. ALDER, *Stochastic event-driven molecular dynamics*, J. Comput. Phys., 227 (2007), pp. 2644–2665.



- [20] J. EGGERS, *Dynamics of liquid nanojets*, Phys. Rev. Lett., 89 (2002), 084502.
- [21] R. F. FOX AND G. E. UHLENBECK, *Contributions to non-equilibrium thermodynamics. I. Theory of hydrodynamical fluctuations*, Phys. Fluids, 13 (1970), pp. 1893–1902.
- [22] A. L. GARCIA, *Nonequilibrium fluctuations studied by a rarefied gas simulation*, Phys. Rev. A, 34 (1986), pp. 1454–1457.
- [23] A. L. GARCIA, *Numerical Methods for Physics*, 2nd ed., Prentice Hall, Englewood Cliffs, NJ, 2000.
- [24] A. L. GARCIA, *Estimating hydrodynamic quantities in the presence of microscopic fluctuations*, Commun. Appl. Math. Comput. Sci., 1 (2006), pp. 53–78.
- [25] A. L. GARCIA AND B. J. ALDER, *Generation of the Chapman-Enskog distribution*, J. Comput. Phys., 140 (1998), pp. 66–70.
- [26] A. L. GARCIA, J. B. BELL, W. Y. CRUTCHFIELD, AND B. J. ALDER, *Adaptive mesh and algorithm refinement using direct simulation Monte Carlo*, J. Comput. Phys., 154 (1999), pp. 134–155.
- [27] A. L. GARCIA, M. MALEK-MANSOUR, G. LIE, AND E. CLEMENTI, *Numerical integration of the fluctuating hydrodynamic equations*, J. Statist. Phys., 47 (1987), p. 209.
- [28] A. L. GARCIA, M. MALEK-MANSOUR, G. C. LIE, M. MARESCHAL, AND E. CLEMENTI, *Hydrodynamic fluctuations in a dilute gas under shear*, Phys. Rev. A, 36 (1987), pp. 4348–4355.
- [29] A. L. GARCIA AND C. PENLAND, *Fluctuating hydrodynamics and principal oscillation pattern analysis*, J. Statist. Phys., 64 (1991), pp. 1121–1132.
- [30] G. GIUPPONI, G. DE FABRITIS, AND P. V. COVENEY, *Hybrid method coupling fluctuating hydrodynamics and molecular dynamics for the simulation of macromolecules*, J. Chemical Physics, 126 (2007), 154903.
- [31] S. GOTTLEIB AND C. SHU, *Total variation diminishing Runge-Kutta schemes*, Math. Comp., 67 (1998), pp. 73–85.
- [32] N. G. HADJICONSTANTINO, *Discussion of recent developments in hybrid atomistic-continuum methods for multiscale hydrodynamics*, Bull. Polish Acad. Sci. Tech. Sci., 53 (2005), pp. 335–342.
- [33] R. D. ASTUMIAN AND P. HANGGI, *Brownian motors*, Physics Today, 55 (2002), pp. 33–39.
- [34] M. KAC, *Foundations of kinetic theory*, in Proceedings of the 3rd Berkeley Symposium on Math. Statist. Probab. Vol. 3, J. Neyman, ed., University of California Press, Berkeley, CA, 1954, pp. 171–197.
- [35] K. KADAU, T. C. GERMANN, N. G. HADJICONSTANTINO, P. S. LOMDAHL, G. DIMONTE, B. L. HOLIAN, AND B. J. ALDER, *Nanohydrodynamics simulations: An atomistic view of the Rayleigh-Taylor instability*, Proc. Natl. Acad. Sci. USA, 101 (2004), pp. 5851–5855.
- [36] K. KADAU, C. ROSENBLATT, J. L. BARBER, T. C. GERMANN, Z. HUANG, P. CARLS, AND B. J. ALDER, *The importance of fluctuations in fluid mixing*, Proc. Natl. Acad. Sci. USA, 104 (2007), pp. 7741–7745.
- [37] W. KANG AND U. LANDMAN, *Universality crossover of the pinch-off shape profiles of collapsing liquid nanobridges in vacuum and gaseous environments*, Phys. Rev. Lett., 98 (2007), 064504.
- [38] G. E. KELLY AND M. B. LEWIS, *Hydrodynamic fluctuations*, Phys. Fluids, 14 (1971), pp. 1925–1931.
- [39] V. I. KOLOBOV, R. R. ARSLANBEKOV, V. V. ARISTOV, A. A. FROLOVA, AND S. A. ZABELOK, *Unified solver for rarefied and continuum flows with adaptive mesh and algorithm refinement*, J. Comput. Phys., 223 (2007), pp. 589–608.
- [40] L. D. LANDAU AND E. M. LIFSHITZ, *Fluid Mechanics*, Course of Theoretical Physics 6, Pergamon, London, 1959.
- [41] A. LEMARCHAND AND B. NOWAKOWSKI, *Fluctuation-induced and nonequilibrium-induced bifurcations in a thermochemical system*, Molecular Simulation, 30 (2004), pp. 773–780.
- [42] M. MALEK-MANSOUR, A. L. GARCIA, G. C. LIE, AND E. CLEMENTI, *Fluctuating hydrodynamics in a dilute gas*, Phys. Rev. Lett., 58 (1987), pp. 874–877.
- [43] M. MALEK-MANSOUR, A. L. GARCIA, J. W. TURNER, AND M. MARESCHAL, *On the scattering function of simple fluids in finite systems*, J. Statist. Phys., 52 (1988), pp. 295–309.
- [44] M. MARESCHAL, M. MALEK-MANSOUR, G. SONNINO, AND E. KESTEMONT, *Dynamic structure factor in a nonequilibrium fluid: A molecular-dynamics approach*, Phys. Rev. A, 45 (1992), pp. 7180–7183.
- [45] P. MEURS, C. VAN DEN BROECK, AND A. L. GARCIA, *Rectification of thermal fluctuations in ideal gases*, Phys. Rev. E (3), 70 (2004), 051109.
- [46] E. MORO, *Hybrid method for simulating front propagation in reaction-diffusion systems*, Phys. Rev. E (3), 69 (2004), 060101.
- [47] M. MOSELER AND U. LANDMAN, *Formation, stability, and breakup of nanojets*, Science, 289 (2000), pp. 1165–1169.

- [48] P. ESPANOL, *Stochastic differential equations for non-linear hydrodynamics*, Phys. A, 248 (1998), pp. 77–96.
- [49] B. NOWAKOWSKI AND A. LEMARCHAND, *Sensitivity of explosion to departure from partial equilibrium*, Phys. Rev. E, 68 (2003), 031105.
- [50] G. OSTER, *Brownian ratchets: Darwin's motors*, Nature, 417 (2002), p. 25.
- [51] J. QIU AND C.-W. SHU, *Runge–Kutta discontinuous Galerkin method using WENO limiters*, SIAM J. Sci. Comput., 26 (2005), pp. 907–929.
- [52] R. SCHMITZ, *Fluctuations in nonequilibrium fluids*, Phys. Rep., 171 (1988), pp. 1–58.
- [53] T. E. SCHWARZENTRUBER, L. C. SCALABRIN, AND I. D. BOYD, *A modular particle-continuum numerical method for hypersonic non-equilibrium gas flows*, J. Comput. Phys., 225 (2007), pp. 1159–1174.
- [54] W. WAGNER, *A convergence proof for Bird's direct simulation Monte Carlo method for the Boltzmann equation*, J. Statist. Phys., 66 (1992), pp. 1011–1044.
- [55] H. S. WIJESINGHE AND N. G. HADJICONSTANTINO, *Discussion of hybrid atomistic-continuum methods for multiscale hydrodynamics*, Internat. J. Multiscale Computational Engineering, 2 (2004), pp. 189–202.
- [56] H. S. WIJESINGHE, R. HORNING, A. L. GARCIA, AND N. G. HADJICONSTANTINO, *Three-dimensional hybrid continuum-atomistic simulations for multiscale hydrodynamics*, J. Fluids Eng., 126 (2004), pp. 768–777.